



Highly dispersed Pt on partial deligandation of Ce-MOFs for furfural selective hydrogenation

Qiuping Yang^a, Daowei Gao^a, Chunsheng Li^{a,*}, Shuai Wang^a, Xun Hu^b, Gengxiu Zheng^{a,*}, Guozhu Chen^{a,*}

^a School of Chemistry and Chemical Engineering, University of Jinan, Jinan, Shandong 250022, PR China

^b School of Material Science and Engineering, University of Jinan, Jinan, Shandong 250022, PR China

ARTICLE INFO

Keywords:

CeO₂
Atomic layer deposition
Metal-organic frameworks
Catalysts

ABSTRACT

Metal-organic frameworks (MOFs) have been extensively investigated as noble metal nanoparticle supports for selective hydrogenations. However, because of small-sized micropores and organic ligands present in MOFs, interactions between inorganic nodes and noble metals are normally weak and the accessibility of active sites is seriously limited. To address these problems, in this study, a partial deligandation strategy is proposed where Pt/CeO₂-270 is obtained by a partial decomposition of Ce-MOFs at 270 °C, then the Pt nanoparticles are deposited by atomic layer deposition (ALD) method. In comparison with the full deligandation of Ce-MOFs at 600 °C (CeO₂-600), the CeO₂-270 catalyst with residual organic ligands exhibits larger surface area, extensive porous structure, abundant Ce³⁺ and oxygen vacancy, which stabilize the highly dispersed small Pt nanoparticles. These unique structural features enable the Pt/CeO₂-270 catalyst to display different furfural (FAL) adsorption configuration, and show excellent FAL conversion (100%) and high selectivity (97.3%) for furfuryl alcohol (FOL). This work provides a strategy to support highly dispersed Pt nanoparticles on MOFs-derived porous materials prepared by partial deligandation strategy, achieving excellent catalytic performance and chemo-selectivity for selective hydrogenation reactions.

1. Introduction

As an important chemical intermediate, furfuryl alcohol (FOL), is widely used as manufacture lubricants, dispersants, and other substances, including lysine and vitamin C [1–5]. FOL can be achieved from the semi-hydrogenation of furfural (FAL), which contains an alkene and carbonyl conjugate bond, as well as furan hetero-cycles. From the thermodynamics viewpoint, the hydrogenation of C=C is advantageous over hydrogenation of C=O [6,7]. Therefore, how to suppress the C=C but boost C=O hydrogenation of FAL is very important yet challenging. Although copper chromate exhibits satisfied selectivity (98% for FOL) in liquid phase at present in different industrial processes, both the toxic Cr₂O₃ and harsh operating conditions (30 bar, 120–200 °C) are highly undesirable [8], hence to drive the search for energy efficient and green catalysts is necessary.

So far, various kinds of metal oxides have been applied to support noble metal nanoparticles, such as Pt, in order to selectively hydrogenate FAL in liquid phase, since the metal oxide supports can be acted as

electron modulator for noble metal nanoparticles [9,10]. For example, a novel hydrotalcite-derived Pt-based catalyst was synthesized to catalyze the selective hydrogenation of FAL to FOL in water. The superior catalytic performance was ascribed to the high dispersion of Pt species, and the selective adsorption of the C=O of FAL on the catalyst. In a recent study, Zhang group constructed a Pt/CeO₂@MOFs catalyst that demonstrated superior catalytic activity toward selective hydrogenation of FAL when compared with Pt@MOFs [11]. CeO₂ is not simply regarded as support, more importantly, its oxygen vacancy as electrophilic site can prefer to adsorb C=O and thus enhance the selectivity. From the support structure viewpoint, porous structure with high surface area would be advantageous for stabilizing noble metal nanoparticles as well as facilitating reactants/products inward/outward diffusion.

In the past decade, metal-organic frameworks (MOFs)-derived metal oxides have attracted considerable interest as supports, because these metal oxides inherit unique structural features of pristine MOFs [12–14]. During the transformation from MOFs into metal oxides, the original spaces within MOFs and the small cavities created by the release

* Corresponding authors.

E-mail addresses: chm_lics@ujn.edu.cn (C. Li), chm_zhenggx@ujn.edu.cn (G. Zheng), chm_chengz@ujn.edu.cn (G. Chen).

<https://doi.org/10.1016/j.apcatb.2023.122458>

Received 21 September 2022; Received in revised form 3 January 2023; Accepted 8 February 2023

Available online 11 February 2023

0926-3373/© 2023 Elsevier B.V. All rights reserved.

of organic ligands and/or solvents are essential to maintain high surface area and abundant pores in metal oxides [15,16]. So far, a large majority of the MOFs-derived metal oxides are achieved by direct calcination of MOFs, however, the destruction of uniform pores and the loss of surface area are inevitable under a high temperature treatment. Hence, there is a balance between surface area and calcination temperature. If the metal oxides are required to maintain high surface area, the calcination temperature should be as low as possible. When the calcination temperature is low, in turn, the MOFs cannot completely decompose and partial organic ligand as a residual would exist. Therefore, one question arises whether the residual organic ligand, if any, affects the catalytic performance.

Since Xu group proposed “quasi-MOFs” in 2018, partial deligandation strategy has been applied to develop structural defects and also generate hierarchical micro- and mesopores [17]. Thanks to this unique structure, Au/MIL-101(573 K) exhibited high activity toward CO oxidation, owing to the accessible Cr-O sites within residual organic ligand, the close contact between Cr-O and Au nanoparticles as well as the large surface area. Additionally, Zhan et al. also found that the porous structure of the Au-Cu/partial deliganded Ce-MOFs catalyst and strong interactions with Au-Cu nanoparticles were vital for its high CO oxidation activity [18]. Considering the residual organic ligands exhibit advantages in some organic substrates-involved catalytic reactions due to their less hydrophilic nature and light weight, it is essential and meaningful to investigate the effect of MOF's partial deligandation on the catalytic performance in liquid reactions, e.g. FAL selective hydrogenation.

In this work, $\text{NH}_2\text{-Ce-BDC}$ was synthesized using 2-amino terephthalic acid ($\text{NH}_2\text{-BDC}$) as organic ligand. Then partial deligandation of cubic $\text{NH}_2\text{-Ce-BDC}$ was achieved by mild pyrolysis at 270°C , followed by loading Pt nanoparticles with ALD technique (Scheme 1). The motivation of choosing 270°C as calcination temperature is due to the following reasons: Firstly, at this low temperature heat-treatment, the organic ligand within $\text{NH}_2\text{-Ce-BDC}$ is not completely removed. Secondly, if the calcination temperature of $\text{NH}_2\text{-Ce-BDC}$ is too low ($<270^\circ\text{C}$), there is a structural change for MOFs during the Pt deposition process. Therefore, the calcination temperature is set as to be 270°C , the same as that of ALD. Because of its high surface area, small sized Pt as well as residual organic ligand, $\text{Pt/CeO}_2\text{-270}$ exhibits higher catalytic performance and FOL selectivity compared with $\text{Pt/CeO}_2\text{-600}$. For the

purpose of investigating the effects of partial/full deligandation toward FAL hydrogenation, XRD, XPS, Raman, HAADF-STEM and in situ DRIFTS were performed.

2. Section for experimentation

2.1. Materials

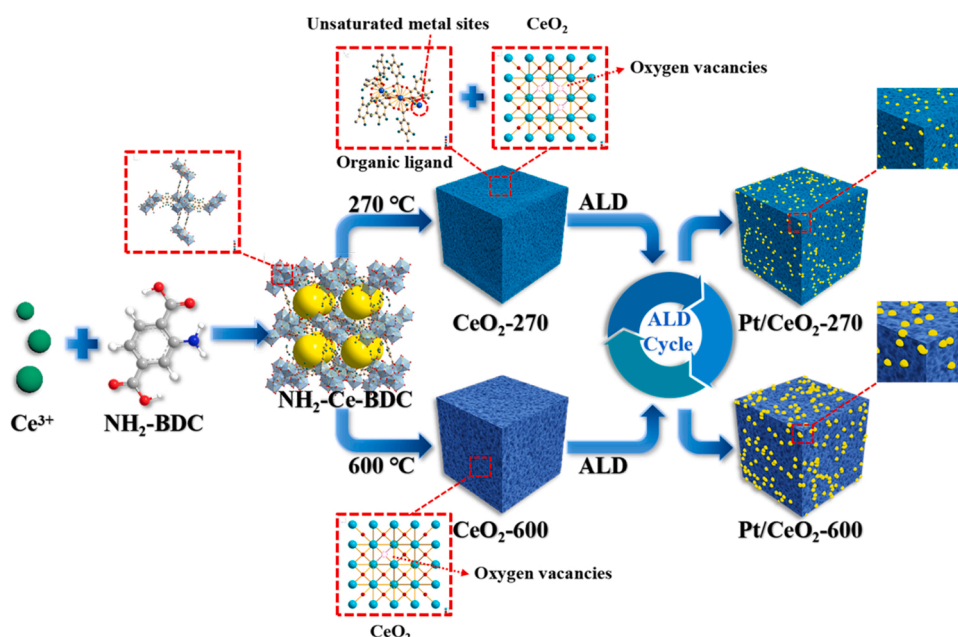
Analytical grade chemicals were used in all experiments. Sinopharm Chemical Reagent Co. Ltd. supplied the ethanol ($\text{CH}_3\text{CH}_2\text{OH}$), sodium hydroxide (NaOH) and cerium chloride heptahydrate ($\text{CeCl}_3 \cdot 7\text{H}_2\text{O}$). Macklin provided 2-amino terephthalic acid. J & K Chemical Co. Ltd. provided (methylcyclopentadienyl)trimethylplatinum (MeCpPtMe_3 , 99%). Furfural was obtained from Shanghai Macklin Biochemical Co. Ltd. The deionized water with a resistance greater than $18\text{ M}\Omega \cdot \text{cm}^{-1}$ was used in the whole experiment.

2.2. Catalyst preparation procedures

The $\text{NH}_2\text{-Ce-BDC}$ was synthesized according to the paper published [19]. Typically, 550 mg of $\text{NH}_2\text{-BDC}$ was dispersed in 110 mL of deionized water in the presence of NaOH . When the pH was set at 5–6, 484 mg of CeCl_3 was added and kept for a while. Following the sample was centrifuged, washed, and dried at 70°C , the $\text{NH}_2\text{-Ce-BDC}$ was obtained. To prepare $\text{CeO}_2\text{-270}$ and $\text{CeO}_2\text{-600}$, $\text{NH}_2\text{-Ce-BDC}$ was heated at 270°C or 600°C for 2 h at a rate of $5^\circ\text{C} \cdot \text{min}^{-1}$ in air. ALD process was performed in an ALD reactor using nitrogen as a carrier gas, which has a hot wall and a closed chamber. ALD was performed by dispersing 50 mg of $\text{CeO}_2\text{-270}$ or $\text{CeO}_2\text{-600}$ in ethanol, dropping it onto the quartz wafer. By sequentially exposed (methylcyclopentadienyl)trimethylplatinum (MeCpPtMe_3) and O_3 at 270°C , Pt was deposited onto $\text{CeO}_2\text{-270}$ or $\text{CeO}_2\text{-600}$. During the deposition process, to ensure adequate vapor pressure, MeCpPtMe_3 was heated to 70°C . The pulse, exposure, and purge times for MeCpPtMe_3 and O_3 were set as 0.1, 10, 25 s, and 1, 10, 25 s, respectively. Through sequentially depositing 20 cycles, $\text{Pt/CeO}_2\text{-270}$ or $\text{Pt/CeO}_2\text{-600}$ was synthesized.

2.3. Characterizations

The phases of the as-obtained catalysts were examined using an X-



Scheme 1. Diagrammatic representation of the fabrication process for the $\text{Pt/CeO}_2\text{-270}$ and $\text{Pt/CeO}_2\text{-600}$.

ray powder diffractometer (XRD) from Japan Rigaku D/Max-RB in a 2θ range of $5\text{--}80^\circ$. High resolution TEM (JEOL 2100 F) equipped with annular dark field detectors and energy dispersive X-ray spectrometers (EDS) as well as scanning electron microscopes (SEM, Hitachi Regulus 8100, Japan) were used to study morphology and structure. Using a Micromeritics Tristar II 3020 instrument at 77 K, the specific surface area for all samples was calculated by Brunauer-Emmett-Teller (BET) method. Before measurements, all samples were pre-treated at 120°C for 12 h. Based on N_2 adsorption data, the pore size distribution was estimated by a Barrett-Joyner-Halenda (BJH) method. H_2 temperature-programmed reduction (H_2 -TPR) was carried out on a chemical adsorption instrument (PCA-1200, Beijing Builder). Typically, the samples for H_2 -TPR were pretreated in flowing Ar (30 mL min^{-1}) at 120°C for 1 h to remove the water, and then conducted from 20 to 1000°C with heating rate of $10^\circ\text{C min}^{-1}$ under the 7% H_2/Ar (30 mL min^{-1}) condition. The thermal property of samples was analyzed by thermogravimetric (STA 449 F5 Jupiter, NETZSCH, Germany) from room temperature to 800°C at a rate of $10^\circ\text{C min}^{-1}$ in air atmosphere. Electron paramagnetic resonance (EPR) was obtained by Bruker EMX plus model spectrometer at 77 K. Chemical compositions and elemental valence of as-prepared samples were characterized by X-ray photoelectron spectroscopy (XPS, ESCALABXi+, Thermo-Fisher) with Al K α radiation as the excitation source. Before XPS characterization, all samples were pre-reduced in H_2 atmosphere. All XPS peaks were calibrated with C1s line at 284.8 eV. The deconvolution was performed on the XPS peak fitting software and the baseline was obtained using Shirley model. Laboratory RAM HR800 with 532 nm excitation laser was used to record Raman spectra. The in situ DRIFTS characterization was characterized using a Bruker Tensor II FTIR spectrometer. The temperature was set at 80°C , and the H_2 flow rate was set as 60 mL min^{-1} . ICP-AES analysis on Thermo Scientific's XSeries-2 was conducted to determine the loading of Pt in the Pt/CeO₂-270 and Pt/CeO₂-600.

2.4. Catalyst performance

The catalytic performance of Pt/CeO₂-270 and Pt/CeO₂-600 was investigated in a stainless steel high-pressure reactor equipped with an attached magnetic stirrer. Selective hydrogenation of FAL was performed to estimate the catalytic properties. A mixture of 10 mg of catalyst and 10 μL of FAL was stirred together in 5 mL of isopropyl alcohol. After flushing air with H_2 completely, 1.0 MPa of H_2 was injected to the autoclave, followed by the heating at 80°C . For the recyclability test, isopropyl alcohol was used to wash the catalyst, and we compensated for the catalyst loss in the subsequent run. After filtering the reaction products, the analyses were performed on a Shimadzu GC-2010 equipped with a Stabilwax column ($30\text{ m} \times 0.25\text{ mm} \times 0.25\text{ }\mu\text{m}$) and flame ionization detector (FID). The column was pre-heated to 50°C for 1 min, then ramped up to 200°C with a rate of $10^\circ\text{C min}^{-1}$ and held for 20 min. The following Eqs. (1) and (2) were used to measure the catalytic selectivity and conversion of FAL:

$$\text{Conversion}(\%) = \frac{\text{Mole of furfural reacted}}{\text{Mole of initial furfural}} \times 100\% \quad (1)$$

$$\text{Selectivity}(\%) = \frac{\text{Mole of furfuryl alcohol}}{\text{Mole of furfural converted}} \times 100\% \quad (2)$$

3. Results and discussion

3.1. Structural characterization

Thermogravimetric analysis (TGA) was firstly performed to check the deligandation behavior of $\text{NH}_2\text{-Ce-BDC}$. As expected, the weight loss of $\text{NH}_2\text{-Ce-BDC}$ gradually decreases as the calcination temperature increases. Based on Fig. 1a, three weight loss stages are obtained. The first weight loss ($<120^\circ\text{C}$) could be assigned to physical adsorption moisture removal from $\text{NH}_2\text{-Ce-BDC}$. The second stage weight loss appears in the

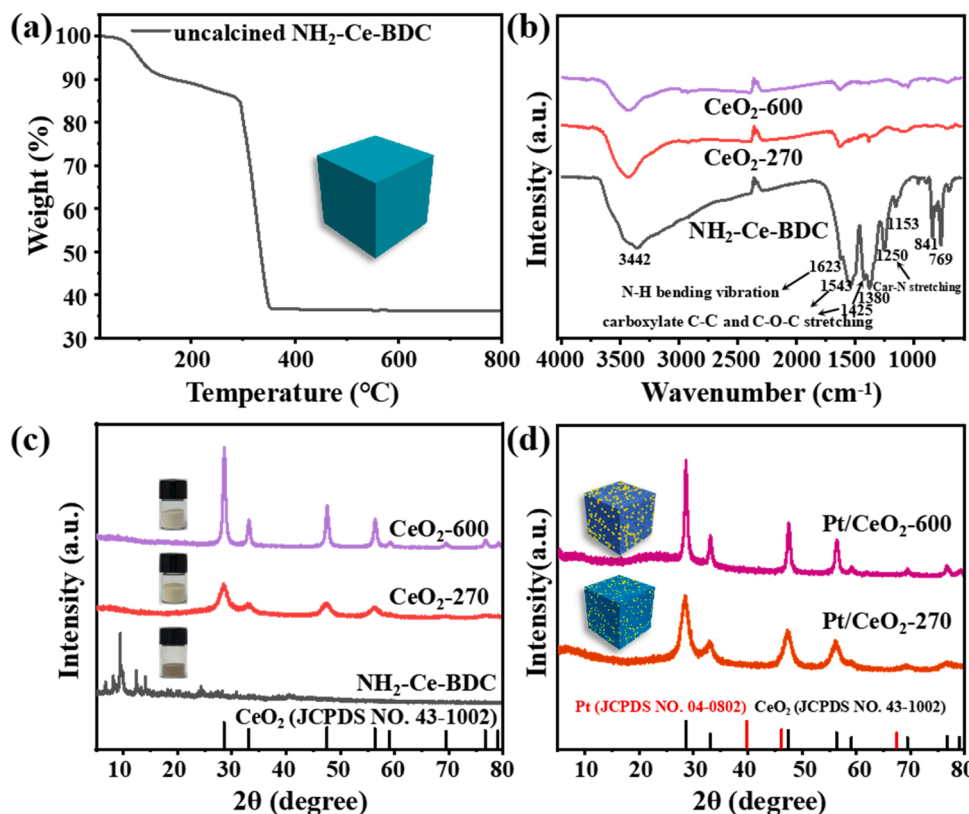


Fig. 1. (a) TG curve of $\text{NH}_2\text{-Ce-BDC}$; (b) FT-IR spectra of uncalcined $\text{NH}_2\text{-Ce-BDC}$, $\text{CeO}_2\text{-270}$, and $\text{CeO}_2\text{-600}$; XRD patterns of uncalcined $\text{NH}_2\text{-Ce-BDC}$, $\text{CeO}_2\text{-270}$, $\text{CeO}_2\text{-600}$ (c) and Pt/CeO₂-270, Pt/CeO₂-600 (d); Insets of (c) show digital photos of the $\text{NH}_2\text{-Ce-BDC}$, $\text{CeO}_2\text{-270}$ and $\text{CeO}_2\text{-600}$.

range of 120–315 °C, due to the partial decomposition of organic ligand. The third stage with sharp weight loss in the range of 315–360 °C is due to the full deligandation and complete decomposition of Ce-MOFs. FT-IR analysis was further conducted to determine whether the organic ligand was removed or not. It is noted that the decomposition curves of NH₂-Ce-BDC are not only affected by calcination temperature, but also affected by dwell time (Fig. S1). For the NH₂-Ce-BDC, the strong peak at 1251 cm⁻¹ is attributed to the C-N deformation vibration [20,21], the ones at 1543, 1425, and 1380 cm⁻¹ are attributed to carboxylic acid groups [22,23]. In addition, the peak at 1623 cm⁻¹ is indexed to N-H bending vibration of -NH₂, while the ones at 841 and 769 cm⁻¹ are associated with the vibrational bending of the Ce-O bond in Ce-MOF [20, 24]. When the calcination condition was set at 270 °C for 2 h, most of the peaks indexed to carboxylic acid and -NH₂ groups disappear, while one peak at 1380 cm⁻¹ is still visible. In comparison, this peak was no longer observed in the case of CeO₂-600, indicating that there is an uncompleted deligandation process at 270 °C for 2 h. Furthermore, Pt/CeO₂-270 exhibited a similar FT-IR spectrum to CeO₂-270, showing that the environment for Pt deposition has no significant effect on the residual organic ligand of CeO₂-270 (Fig. S2).

XRD was used to investigate the crystal structure change after calcination. Fig. 1c shows the diffraction pattern of NH₂-Ce-BDC with the sharp and intense peaks in the range of 5 and 20°. As discussed above, the decomposition degree of NH₂-Ce-BDC is dependent on the calcination temperature and dwell time, which is further verified by XRD pattern (Fig. S3). Specifically, after calcination either at 270 °C or 600 °C, there are no characteristic peaks of NH₂-Ce-BDC, even CeO₂-270 sample retains non-ignorable residual organic ligand. Instead, (111), (200), (220), (222), (400), (331) and (420) diffraction peaks of the face-centered-cubic fluorite CeO₂ phase are clearly discernible (JCPDS card No. 43-1002). Due to the low temperature calcination, the half-width of these diffraction peaks of CeO₂-270 are wider than those of CeO₂-600, indicating the former one exhibits smaller CeO₂ crystalline size. After Pt loading, no distinguished Pt diffraction peaks were detected, possibly due to its high dispersion.

3.2. Morphological characterization

A scanning electron microscope (SEM) and high-resolution transmission electron microscopy (HRTEM) were used to characterize the morphology characteristics of the obtained Pt/CeO₂ (Fig. 2). As illustrated in Fig. S4, an average length of approximately 3.5 μm is observed for NH₂-Ce-BDC, which exhibits cubic morphology with a smooth surface. Instead, when the H₂BDC was used as organic linker, the as-prepared Ce-MOF is random in morphology (Fig. S5). After thermal treatment of NH₂-Ce-BDC at 270 °C, the surface of CeO₂ became relatively rough while the cubic structure was preserved and no significant size changes were observed (Fig. S6 a-c). It is reasonable that a large number of pores on the surface are formed because of the organic ligand release during the calcination process. By increasing the temperature to 600 °C, the as-prepared CeO₂-600 still exhibited a similar cubic structure, however, the pores on its surface are larger compared to those of CeO₂-270 (Fig. S6 d-f). The creation of larger pores is related to the full deligandation and complete decomposition of NH₂-Ce-BDC at 600 °C. After Pt deposition by ALD, there are no distinct changes in morphology and size from SEM images (Fig. 2 and Fig. S7-S8). Taking Pt/CeO₂-270 as an example, the pores can be still observed. From HRTEM and HAADF images, Pt nanoparticles with a diameter of ~2.6 nm are well dispersed over CeO₂-270, where the interlayer spacing of ~0.31 and ~0.27 nm could be assigned to (111) and (200) of CeO₂, respectively, and the ~0.23 nm is corresponding to (111) of Pt. The diffraction rings of (111), (200), (220), (311) and (400) of CeO₂ are clearly identified in the selected area electron diffraction (SAED) pattern. Elemental mapping (Fig. 2h), elemental line scanning profile image (Fig. S9) and energy dispersive spectroscopy (EDS) (Fig. S10) further confirmed the presence of Pt. Despite the identical deposition cycles (20 ALD cycles) and similar loading amount (estimated by ICP-MS as 2.96 wt% for Pt/CeO₂-270 and 2.86 wt% for Pt/CeO₂-600), the Pt nanoparticles in Pt/CeO₂-600 are not uniform and have a larger particle size of 3.1 ± 0.25 nm in comparison to Pt/CeO₂-270 (Fig. S11).

3.3. Surface area and pore size analysis

Fig. 3 shows the N₂ adsorption-desorption isotherms for CeO₂-270

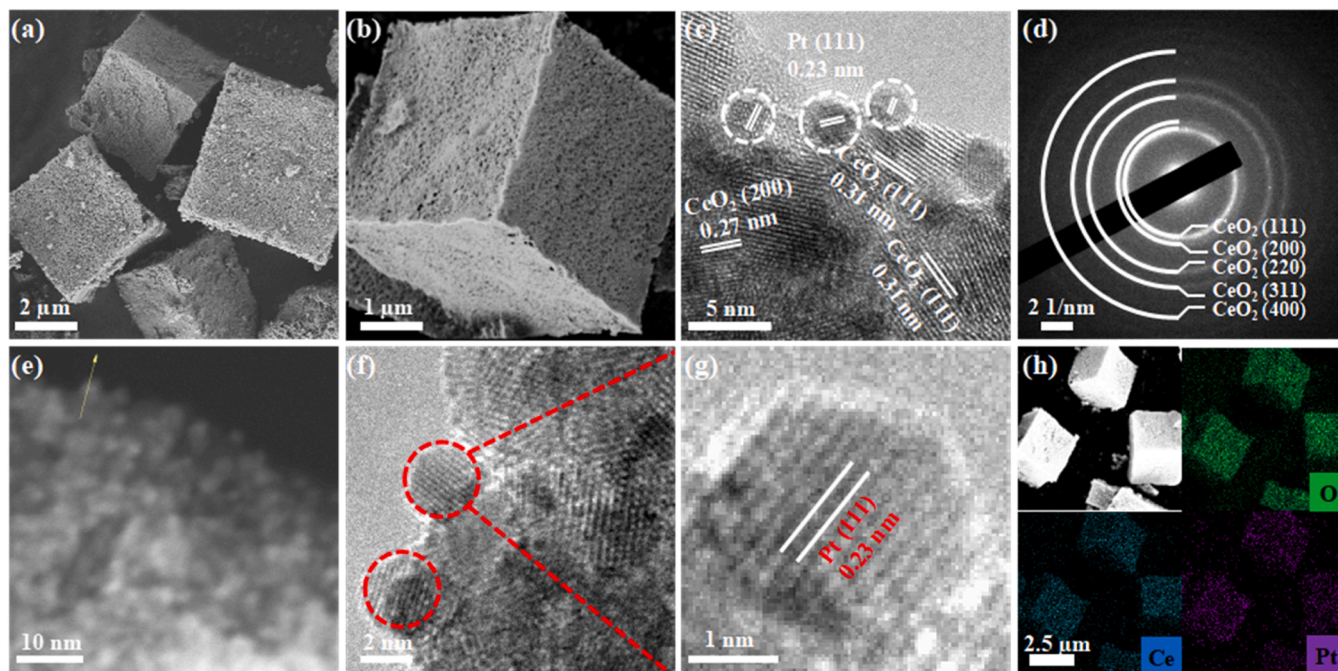


Fig. 2. SEM (a, b), HRTEM/STEM (c, e-g), SAED (d), and elemental mapping images (h) of Pt/CeO₂-270.

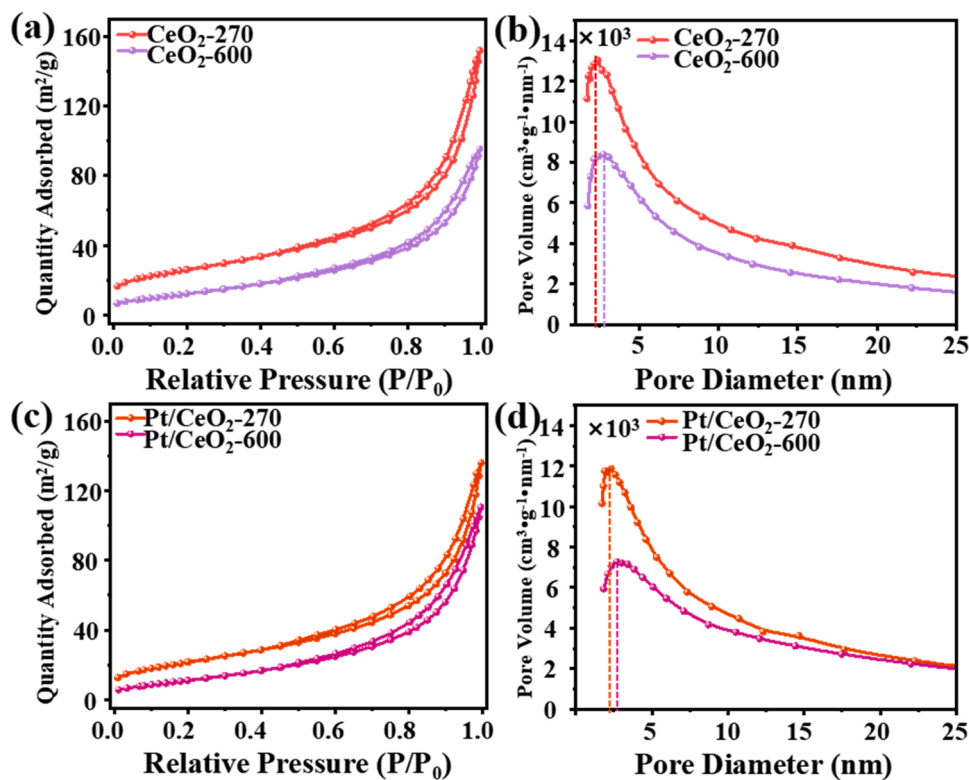


Fig. 3. Isotherms of nitrogen adsorption and pore size distributions of CeO_2 -270, CeO_2 -600, Pt/CeO_2 -270 and Pt/CeO_2 -600.

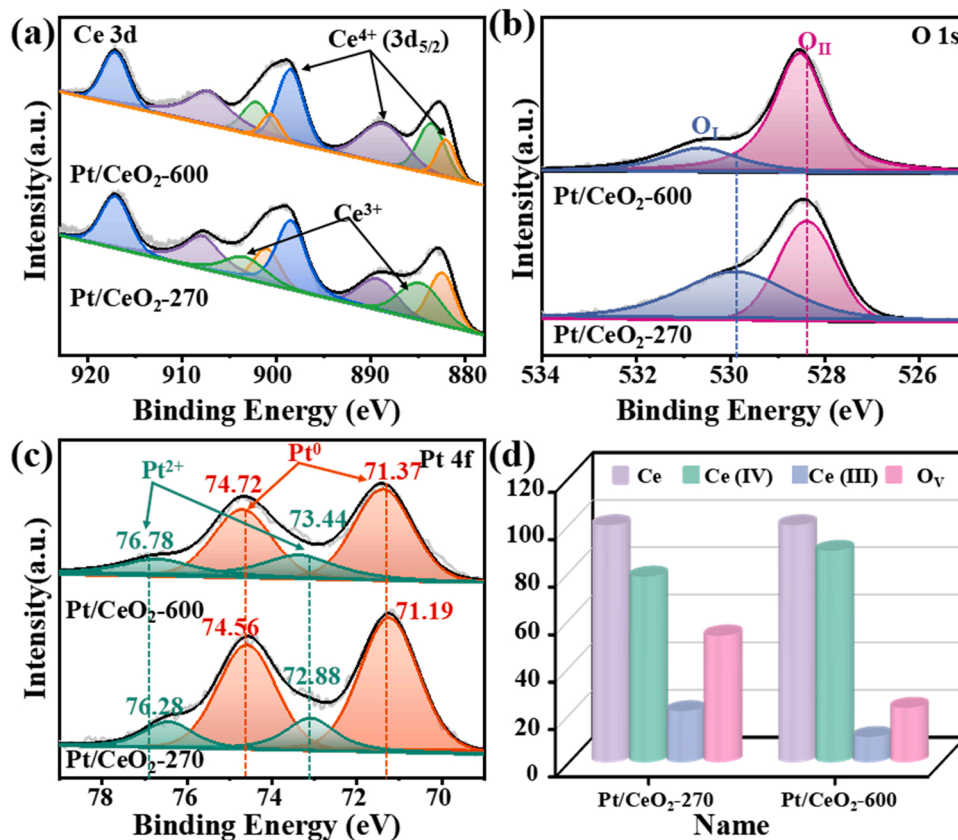


Fig. 4. (a), (b), and (c) are XPS spectra of Ce 3d, O 1s and Pt 4f of Pt/CeO_2 -270 and Pt/CeO_2 -600, respectively, and (d) is the relative amount of Ce^{3+} , Ce^{4+} , and O_V of Pt/CeO_2 -270 and Pt/CeO_2 -600.

and CeO₂-600, along with Pt/CeO₂-270, and Pt/CeO₂-600, to provide a further understanding of the differences in the structural features of the prepared samples. A characteristic H₃ hysteresis loop was observed in both CeO₂ and Pt/CeO₂. Based on BET measurements, CeO₂-270 has a specific surface area of 92.24 m²/g, and the pore size mainly locates at ~3 nm. Comparatively, CeO₂-600 has a specific surface area of 47.20 m²/g, almost half of CeO₂-270, and its pore size increases to ~4 nm. CeO₂-270 has a large surface area, which is certainly beneficial for high dispersion of Pt nanoparticles. Upon Pt deposition, the surface area of Pt/CeO₂-270 decreases to 78.22 m²/g, and the one of Pt/CeO₂-600 decreases to 45.11 m²/g as well (Table S1). The pore volume and pore size distribution show almost no difference, demonstrating the Pt nanoparticles deposited on CeO₂ do not block the pores either. Keeping in mind that the Pt deposition procedures are totally the same, the differences in Pt particle size and uniformity from HRTEM results are largely related to their different structural features between CeO₂-270 and CeO₂-600.

3.4. Chemical states and elemental composition analysis

To analyze the chemical composition and elemental states of Pt, Ce, and O in Pt/CeO₂-270 and Pt/CeO₂-600, the XPS technique was performed. The Ce 3d XPS spectra comprised two distinct types of Ce species, as illustrated in Fig. 4a. Specifically, the position peaks at 882.05, 900.58, 888.83, 907.44, 898.65, and 917.18 eV are indexed to Ce(IV) species, the ones at 883.66, 902.20, 885.07, and 903.81 eV are corresponding to Ce(III). Based on the deconvolution result, the proportion of Ce(III) of Pt/CeO₂-270 and Pt/CeO₂-600 was calculated to be 21.69% and 10.79%, respectively. In general, there is a close relationship between the content of Ce(III) and that of O: the more Ce(III) ceria contains, the higher content of oxygen vacancy ceria has. As shown in Fig. 4b, there are two peaks at around 528.41 and 530.16 eV,

corresponding to the surface oxygen-containing species (i.e., hydroxyl-like groups or oxygen vacancies) or defect-oxide (O_I) and lattice oxygen (O_{II}), respectively. Obviously, the Pt/CeO₂-270 accommodates more O_I than that of Pt/CeO₂-600. It is well-recognized that the defects can facilitate the nucleation of deposited noble metal nanoparticles, and stabilize them as well. The electron paramagnetic resonance (EPR) was performed to verify the existence of oxygen vacancy (Fig. S12). The higher intensity of EPR signal for Pt/CeO₂-270 indicates its more abundant oxygen vacancies than that of Pt/CeO₂-600. Therefore, the Pt nanoparticles supported onto CeO₂-270 exhibit smaller size compared with ones onto CeO₂-600, as observed from HRTEM images. There are two pairs of doublets in Pt 4f spectra, corresponding to metallic Pt⁰ and Pt²⁺ species, which can be deconvoluted to Pt 4f_{7/2} and Pt 4f_{5/2} spin-orbit components. Compared with Pt/CeO₂-600, the lower binding energy and higher proportion of surface Pt⁰ species are achieved for Pt/CeO₂-270.

3.5. Concentration of surface oxygen vacancies, reduction behavior and CO-DRIFTS analysis

As shown in Fig. 5a, Raman spectra of Pt/CeO₂-270 and Pt/CeO₂-600 are compared. For CeO₂, Ce-O symmetric stretching vibration (F_{2g}) is indexed to the peak at 458 cm⁻¹ [25]. Another peak at 597 cm⁻¹ is ascribed to the defected-induced mode (ID) because of the presence of Ce³⁺ [25]. As demonstrated in Fig. S13, the value of I₅₉₇/I₄₆₀ is used to calculate oxygen vacancy concentration. CeO₂-270 catalyst contains 3.36 times more oxygen vacancies than that of CeO₂-600. After Pt deposition by ALD, there are two new peaks, especially for Pt/CeO₂-270, which are corresponding to the Pt-O-Ce bridging vibration and Pt-O vibration of the Pt-O-Ce bond, respectively (Fig. 5a) [26]. Besides, for Pt/CeO₂-600 and Pt/CeO₂-270, the F_{2g} peak red-shifts from 458 cm⁻¹ to 455 cm⁻¹, respectively (Fig. S14). The more broadening peak in the

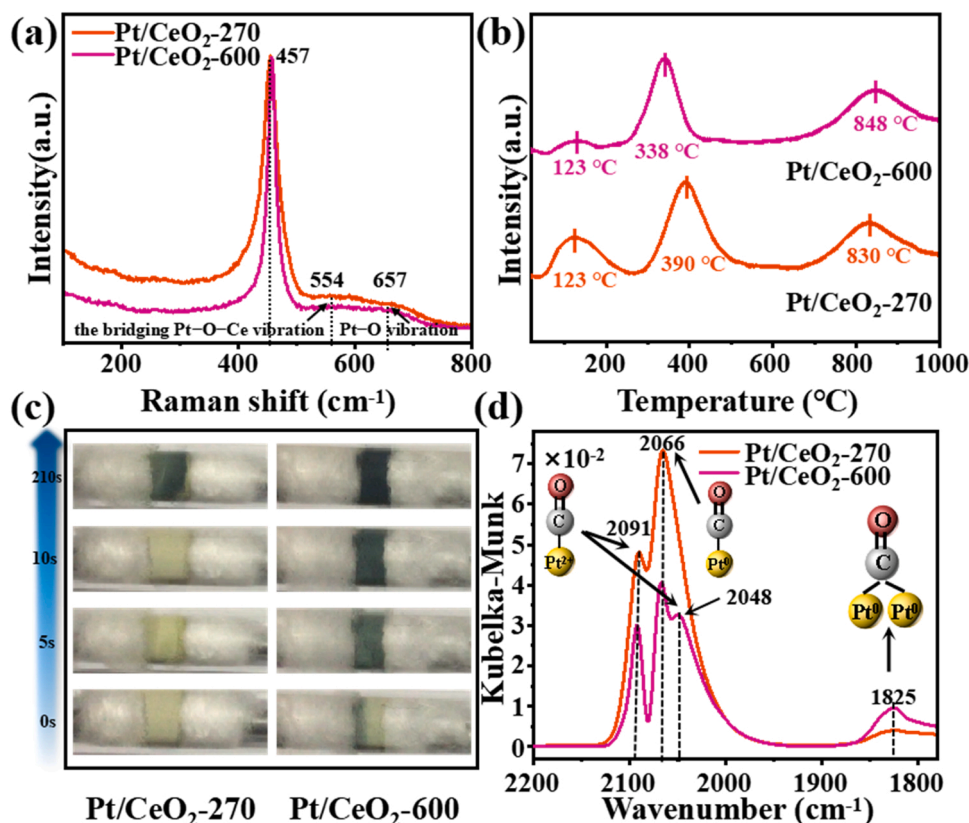


Fig. 5. (a) Raman spectra of Pt/CeO₂-270 and Pt/CeO₂-600; (b) H₂-TPR spectra of Pt/CeO₂-270 and Pt/CeO₂-600; (c) Digital photographs of catalysts containing 200 mg of WO₃ and 20 mg Pt/CeO₂-270 and Pt/CeO₂-600 after treatment with H₂ at 0 s, 5 s, 10 s and 210 s; (d) CO-DRIFTS spectra of Pt/CeO₂-270 and Pt/CeO₂-600.

latter is due to the existence of more oxygen vacancies and Ce^{3+} that induces disorder and decreases the Ce-O bond strength.

The H_2 -TPR technique was applied to investigate the reduction behavior of Pt/CeO₂-270 and Pt/CeO₂-600 catalysts. As shown in Fig. 5b, for Pt/CeO₂-270 and Pt/CeO₂-600 catalysts, three peaks in the temperature range of 25–1000 °C were observed at 123–126 °C, 338–390 °C, and 830–854 °C respectively. The peak located at 123–126 °C, PtO_x is being reduced, while in the peak at 300–500 °C, active oxygen close to the surfaces between Pt and CeO₂ is being reduced [27–29]. The peak appeared at 830–854 °C is caused by oxygen reduction in the CeO₂ bulk lattice. In the range of 123–126 °C, Pt/CeO₂-270 consumes more hydrogen than Pt/CeO₂-600. As concluded above, more dispersed and smaller Pt particles are supported on CeO₂-270, which results in more amount of Pt species is reduced, causing higher consumption of hydrogen. It is well documented that the decrease of active oxygen at lower temperature is facilitated by the H₂ overflow from the reduced Pt sites to CeO₂ [30]. The reduction peak of active oxygen adjacent to Pt should be located at a lower temperature because of the high dispersion and tiny size of Pt present in Pt/CeO₂-270. However, Pt/CeO₂-270 displayed more than 50 °C higher than that of Pt/CeO₂-600 for oxygen reduction peak, suggesting H₂ spillover effect is more obvious for Pt/CeO₂-600 [31]. As confirmed by WO₃ color change experiment in Fig. 5c, the color of the mixture of Pt/CeO₂-600 and WO₃ changes within 5 s, faster than that of Pt/CeO₂-270. The inferior H₂ spillover ability is probably due to the presence of residual organic ligand in Pt/CeO₂-270.

As shown in Fig. 5d, the CO-DRIFTS technique was employed to compare the Pt species. It was assumed that the 2091 cm⁻¹ peak was a result of CO adsorption onto small oxidized Pt clusters (atomically dispersed Pt) [29,30,32,33]. The peak at 2066 cm⁻¹ can be attributed to the Pt clusters linearly bonded CO [34]. Obviously, the peak intensity in the range of 2048–2093 cm⁻¹ for Pt/CeO₂-270 are greater than those of Pt/CeO₂-600, which can be explained by the high dispersion and the

larger proportion of Pt clusters in the former sample. Noticeably, the peak at 1825 cm⁻¹, indicating of CO adsorption on large Pt particles [35–37], is stronger for Pt/CeO₂-600 than that of Pt/CeO₂-270, which is in agreement with the HRTEM result.

3.6. Catalytic evaluations toward furfural selective hydrogenation

The results of the investigation into the catalytic performances of Pt/CeO₂-270 and its counterpart Pt/CeO₂-600 in the selective hydrogenation of FAL are shown in Fig. 6a and b. For Pt/CeO₂-270, 100% of FAL conversion and 97.3% of FOL selectivity were reached within 60 min. In contrast, although 100% conversion can be achieved within 80 min in the case of Pt/CeO₂-600, the FOL selectivity is significantly different. Specifically, Pt/CeO₂-270 showed a selectivity of 97.3% toward FOL at 60 min, which maintained above 96.0% within 120 min, indicating that Pt/CeO₂-270 catalyst preferentially hydrogenates C=O and effectively suppresses further hydrogenation in the furan ring of FOL, leading to high FOL selectivity. Conversely, in the case of Pt/CeO₂-600 catalyst, although the selectivity of FOL could reach 97% at the beginning of the reaction (0–60 min), it drastically dropped in the following 40 min, and decreased to 83.9% at 120 min. Obviously, the Pt/CeO₂-270 catalyst exhibits better catalytic performance in FOL selectivity and yield (Fig. 6c, Table S2). Noticeably, either Pt/CeO₂-270 or Pt/CeO₂-600 displays higher catalytic activity and selectivity than that of Pt/CeO₂ (commercial) (Fig. S15), demonstrating the advantageous structure of MOF-derived catalysts in catalytic reactions. The calculated TOF value reaches as high as 778 h⁻¹, which is better than most reported values (Table S3). Furthermore, the recycling tests were conducted on Pt/CeO₂-270 to determine its stability and recyclability. As shown in Fig. 6d, the conversion activity and selectivity remained at 99.11% and 96.52% after five consecutive runs. The morphology, structure and surface composition of the used catalysts were investigated by SEM, XRD and FT-IR (Fig. S16–18). Clearly, there are no obvious changes compared

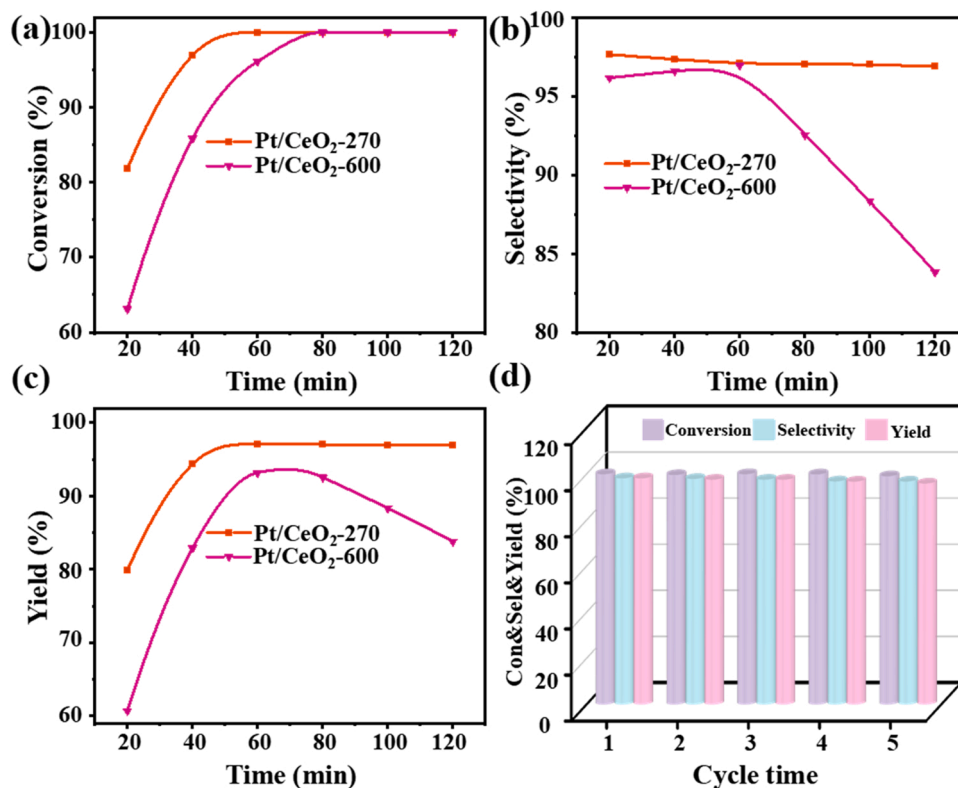


Fig. 6. (a) Catalysis of FAL conversion on Pt/CeO₂-270 and Pt/CeO₂-600 versus reaction time; (b) Comparison of Pt/CeO₂-270 and Pt/CeO₂-600 catalyst selectivity versus reaction time; (c) Yields for Pt/CeO₂-270 and Pt/CeO₂-600 samples plotted against reaction time; (d) Recyclability of Pt/CeO₂-270 under selective hydrogenation with FAL.

with fresh ones, demonstrating good stability and recyclability of Pt/CeO₂-270 catalyst.

3.7. Mechanism of furfural selective hydrogenation

Determining the adsorption behavior of FAL on catalysts can help us to understand the catalytic performance differences. As displayed in Fig. 7a and Fig. S19, the peaks located at 1648–1698 cm⁻¹ could be ascribed to C=O stretching and vibration [38–41], and the peaks at 1455–1465 cm⁻¹ and 1580–1591 cm⁻¹ were assigned to C=C characteristic vibrations and furan ring breath, respectively [39,40,42]. The peaks at 1150–1270 cm⁻¹ were indexed to C-O, C-C stretching vibration and C-H bending vibration within the furan ring [38,40]. Keeping in mind that when the furan ring becomes chemically bound to the catalyst surface, those peaks indexed to $\nu(\text{C}=\text{O})$ and furan ring breath would disappear. In other words, the emergence of these peaks exists only when the furan ring is physically adsorbed [43]. Obviously, the peaks at 1150–1575 cm⁻¹ are stronger for Pt/CeO₂-270 than those of Pt/CeO₂-600, indicating that the furan ring is not chemically adsorbed in the former catalyst. Meanwhile, the strong FAL adsorption with free and unconstrained state of Pt/CeO₂-270 is possible due to the catalyst contains rich defect sites as well as residual organic ligand. Compared with the $\nu(\text{C}=\text{O})$ of gas phase FAL, a significant red-shift in $\nu(\text{C}=\text{O})$ from 1670 cm⁻¹ to 1643 cm⁻¹ for Pt/CeO₂-270 and Pt/CeO₂-600 samples, demonstrating that C=O is linear chemical adsorbed in a $\eta^1(\text{O})$ configuration for both catalysts [38,40]. However, in addition to C=O

chemical adsorption, C=C bridge chemical adsorption also exists for Pt/CeO₂-600 due to the absence of furan ring breath and $\nu(\text{C}=\text{C})$ (Fig. S20). Therefore, the production of tetrahydrofurfuryl alcohol (THFOL) was observed for Pt/CeO₂-600 as a consequence of the full hydrogenation of FAL, while only C=O bond activation adsorption favors semi-hydrogenation and increases FOL selectivity in the case of Pt/CeO₂-270 (Fig. S21).

During the semi-hydrogenation catalytic process, when the intermediates are hard to leave, it becomes highly possible that the over-hydrogenation occurs. As the semi-hydrogenation product, FOL's desorption behaviors on different catalysts are therefore compared. According to Fig. 7b, the peaks at 1098 and 1045 cm⁻¹ were ascribed to $\sigma(\text{C}-\text{O})$ and $\gamma(-\text{CH}_2)$ [42], respectively. In the cases of Pt/CeO₂-270, the intensity of $\sigma(\text{C}-\text{O})$ and $\gamma(-\text{CH}_2)$ abruptly decreased upon continuous N₂ purging. In contrast, the intensity of those two peaks displayed a relatively slow descent for Pt/CeO₂-600. The normalized desorption rate curves verified a much faster detachment of FOL from Pt/CeO₂-270 than that from Pt/CeO₂-600 (Fig. S22), further explaining why the Pt/CeO₂-270 exhibits high selectivity for FOL.

Besides, in situ DRIFTS spectra were provided to understand the catalytic reaction mechanism by monitoring the accumulation and decline of various bands. As shown in Fig. 8, in situ DRIFTS spectra were observed for FAL selective hydrogenation with purging H₂ for 2, 4, 6, 8, and 10 min. It is clear that the strong characteristic peaks assigned to C=O declines faster, while C-OH (1078 cm⁻¹) increases faster for Pt/CeO₂-270 with the continuous inflow of H₂ than those of Pt/CeO₂-600,

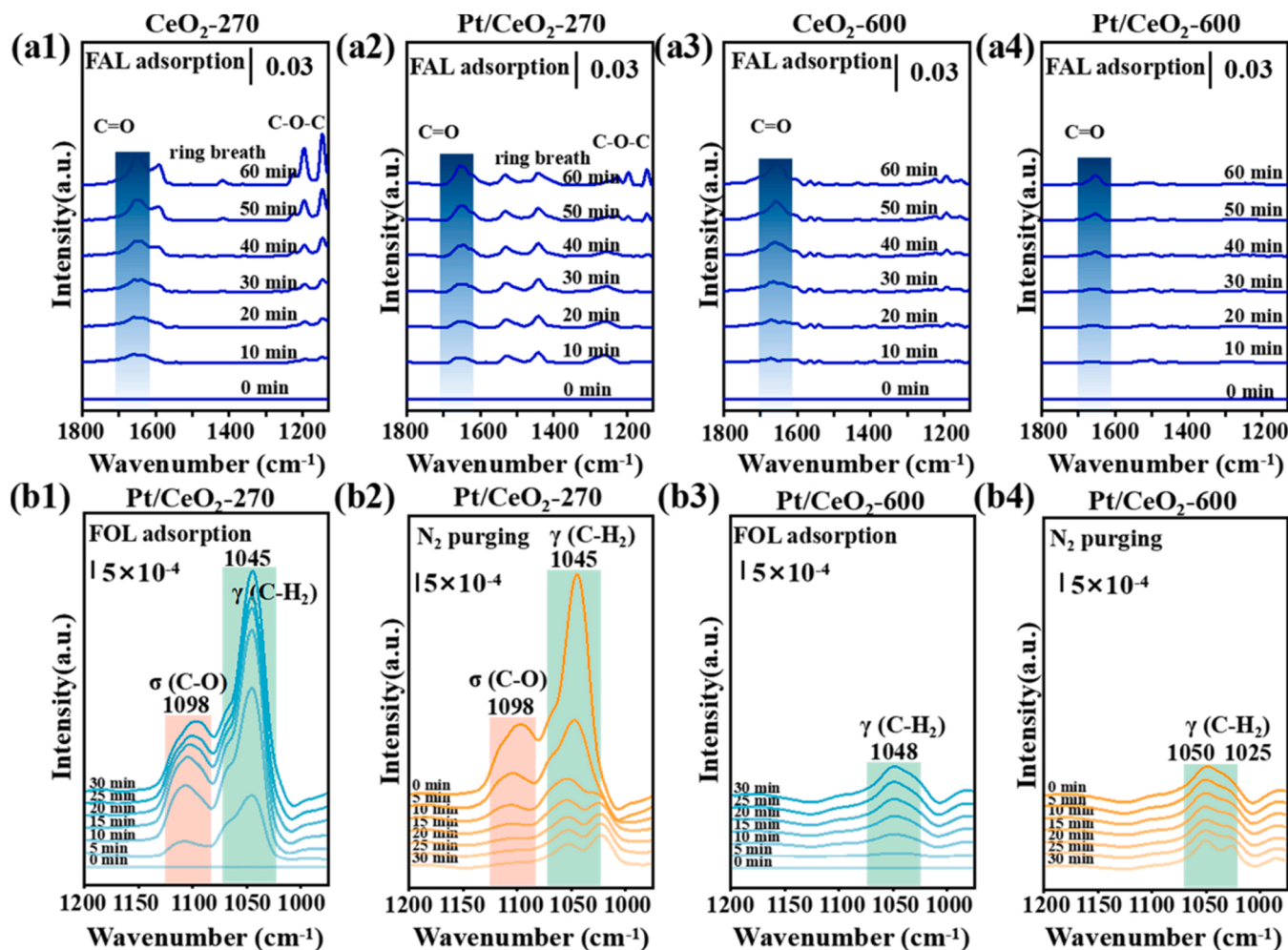


Fig. 7. (a1-a4) FAL-DRIFTS spectra of CeO₂-270, CeO₂-600, Pt/CeO₂-270 and Pt/CeO₂-600 samples; (b1-b4) *In situ* DRIFTS spectra of FOL desorption from (a) Pt/CeO₂-270 and (b) Pt/CeO₂-600 upon continuous N₂ purging.

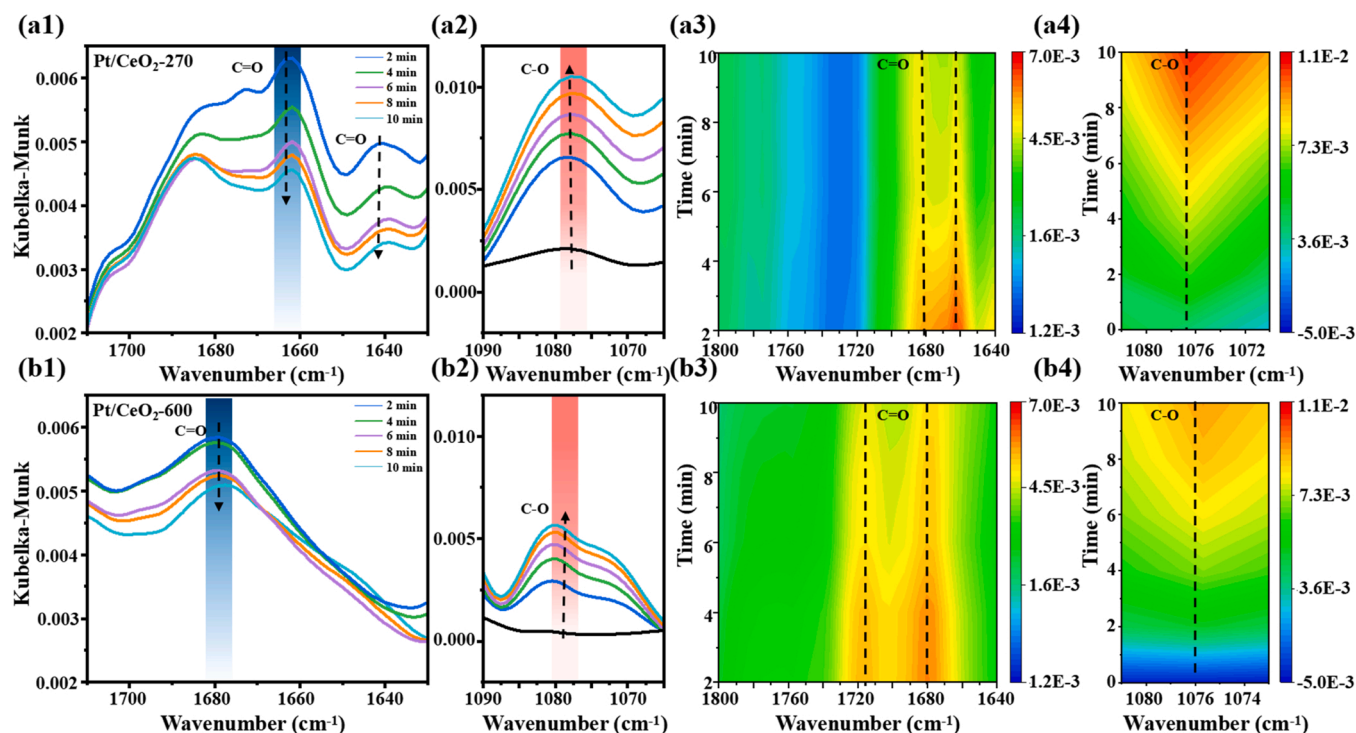
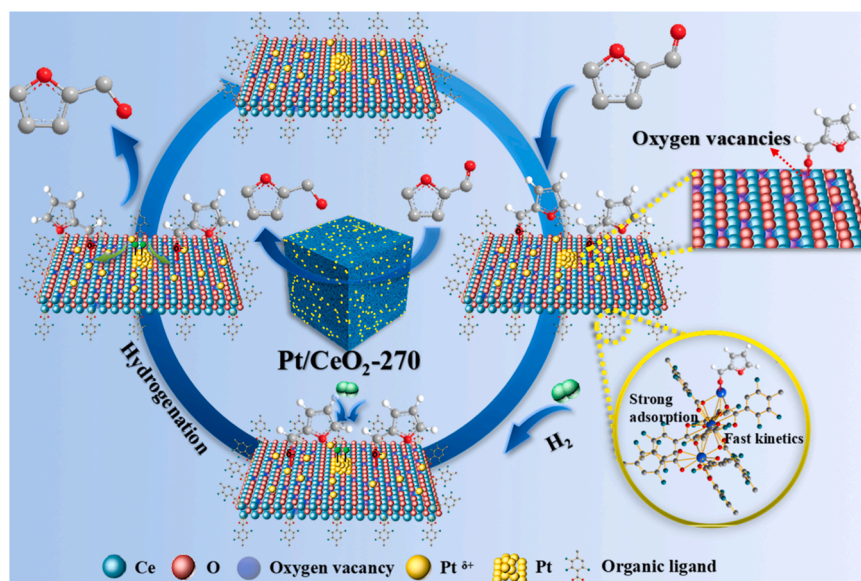


Fig. 8. *In situ* DRIFTS spectra for the hydrogenation of FAL using flowing H_2 as the reaction gas on (a) Pt/CeO₂-270 and (b) Pt/CeO₂-600.

indicating the higher catalytic activity of Pt/CeO₂-270 within the initial 10 min. This tendency was also reflected by three-dimensional diagram of peak intensity evolution over time, in which the color difference shows that the Pt/CeO₂-270 catalyst performs superior catalytic activity.

Based on the above discussion, Pt/CeO₂-270 showed better FAL activity and C=O hydrogenation selectivity compared with Pt/CeO₂-600. The high activity was contributed by a larger specific BET surface area and pore volume of Pt/CeO₂-270. The high specific BET surface area was beneficial for Pt nanoparticle uniform dispersion. Meanwhile, the porosity structure of Pt/CeO₂-270 enhanced the accessibility of active sites with the reactant as well as improved the diffusion of substrate and products, thus leading to excellent catalytic performance. Besides, the partial ligand removal was beneficial to creating structural defects and

unsaturated metal sites, a new chance to enhance interactions between the guest species, including Pt and FAL. Thus, different structural features between Pt/CeO₂-270 and Pt/CeO₂-600 render different FAL adsorption configuration. In addition, the presence of abundant Ce³⁺ and oxygen vacancy of Pt/CeO₂-270 can serve as Lewis acid sites or electrophilic sites to adsorb, polarize, and activate the electron-rich C=O bonds by donating an electron to the oxygen atom (electron-donating group). Last but not least, the residual ligand enables the CeO₂-270 to exhibit a larger contact angle between its surface and liquid water (Fig. S23). The more hydrophobic feature of CeO₂-270 is absolutely advantageous for FAL adsorption. FAL hydrogenation over Pt/CeO₂-270 is described in a possible mechanism, as shown in Scheme 2.



Scheme 2. Possible hydrogenation mechanism for FAL over Pt/CeO₂-270.

4. Conclusions

In summary, we have synthesized Pt/CeO₂ catalysts, in which the CeO₂ was derived from partial/full deligandation of NH₂-Ce-BDC, and Pt nanoparticles were loaded by ALD technique. Owing to the low temperature (270 °C) treatment for partial deligandation, the Pt/CeO₂-270 catalyst exhibits different structural features, which also enable it to display higher catalytic performance, i.e., an excellent selectivity of 97.3% at 100% FAL conversion in comparison to Pt/CeO₂-600. This excellent catalytic performance can be contributed to (1) the larger specific BET surface area, which is advantageous for the uniform dispersion of nanoparticles. (2) Porous structure, which could enhance active sites accessibility with the reactant as well as improve the in-/outward diffusion of substrates and products. (3) Pt and CeO₂ have a strong interaction, which could modify its surface density and d-band center. (4) Abundant Ce³⁺ and oxygen vacancy could stabilize Pt nanoparticles as well as serve as electrophilic sites or Lewis acid sites for C=O adsorption. (5) Residual organic ligands are beneficial for furfural adsorption. Obviously, this work manifests an avenue to design efficient hydrogenation catalysts by choosing partial/full deligandation of MOF for supporting noble metal nanoparticles.

CRediT authorship contribution statement

Qiuping Yang: Validation, Formal analysis, Investigation, Resources, Data curation, Writing – original draft. **Daowei Gao:** Validation, Formal analysis, Supervision. **Chunsheng Li:** Validation, Supervision. **Shuai Wang:** Resources. **Xun Hu:** Validation, Supervision. **Gengxiu Zheng:** Conceptualization, Methodology, Validation, Supervision. **Guozhu Chen:** Conceptualization, Methodology, Validation, Formal analysis, Supervision, Writing – review & editing, Project administration.

Declaration of Competing Interest

The authors declare that they have no known competing financial interests or personal relationships that could have appeared to influence the work reported in this paper.

Data availability

No data was used for the research described in the article.

Acknowledgments

This work was financially supported by National Natural Science Foundation of China (Grant No. 21878121), Jinan Science and Technology Bureau (2021GXRC086), and Shandong Provincial Natural Science Foundation (Grant No. ZR202102230042).

Appendix A. Supporting information

Supplementary data associated with this article can be found in the online version at [doi:10.1016/j.apcatb.2023.122458](https://doi.org/10.1016/j.apcatb.2023.122458).

References

- W.L. Xu, C.J. Yu, J.Z. Chen, Z.Y. Liu, Electrochemical hydrogenation of biomass-based furfural in aqueous media by Cu catalyst supported on N-doped hierarchically porous carbon, *Appl. Catal. B Environ.* 305 (2022), 121062.
- Y. Zou, M.K. Zhang, Y.X. Liu, Y.Y. Ma, S. Zhang, Y.Q. Qu, Highly selective transfer hydrogenation of furfural into furfuryl alcohol by interfacial frustrated lewis pairs on CeO₂, *J. Catal.* 410 (2022) 54–62.
- M.J. Taylor, S.K. Beaumont, M.J. Islam, S. Tsatsos, C.A.M. Parlett, M.A. Isaacs, G. Kyriakou, Atom efficient PtCu bimetallic catalysts and ultra dilute alloys for the selective hydrogenation of furfural, *Appl. Catal. B Environ.* 284 (2021), 119737.
- Q. Fu, X. Xu, R. Miao, M. Wang, H. Zhou, L. He, Q. Guan, Mn-embedded porous rubber seed shell biochar for enhanced removal of copper ions and catalytic efficacy of the used adsorbent for hydrogenation of furfural, *Chem. Eng. J.* 441 (2022), 136065.
- Y. Fan, S. Li, Y. Wang, C. Zhuang, X. Liu, G. Zhu, X. Zou, Tuning the synthesis of polymetallic-doped ZIF derived materials for efficient hydrogenation of furfural to furfuryl alcohol, *Nanoscale* 12 (2020) 18296–18304.
- Z. Zhao, R. Bababrik, W. Xue, Y. Li, N.M. Briggs, D.-T. Nguyen, U. Nguyen, S. P. Crossley, S. Wang, B. Wang, Solvent-mediated charge separation drives alternative hydrogenation path of furanics in liquid water, *Nat. Catal.* 2 (2019) 431–436.
- X.C. Lan, T.F. Wang, Highly selective catalysts for the hydrogenation of unsaturated aldehydes: a review, *ACS Catal.* 10 (2020) 2764–2790.
- A. Corma, S. Iborra, A. Velty, Chemical routes for the transformation of biomass into chemicals, *Chem. Rev.* 107 (2007) 2411–2502.
- G. Gao, J. Remón, Z. Jiang, L. Yao, C. Hu, Selective hydrogenation of furfural to furfuryl alcohol in water under mild conditions over a hydrothermalite-derived Pt-based catalyst, *Appl. Catal. B Environ.* 309 (2022), 121260.
- M.J. Taylor, L.J. Durnell, M.A. Isaacs, C.M.A. Parlett, K. Wilson, A.F. Lee, G. Kyriakou, Highly selective hydrogenation of furfural over supported Pt nanoparticles under mild conditions, *Appl. Catal. B Environ.* 180 (2016) 580–585.
- Y. Long, S. Song, J. Li, L. Wu, Q. Wang, Y. Liu, R. Jin, H. Zhang, Pt/CeO₂@MOF core@shell nanoreactor for selective hydrogenation of furfural via the channel screening effect, *ACS Catal.* 8 (2018) 8506–8512.
- L. Huang, F. Hao, Y. Lv, Y. Liu, P. Liu, W. Xiong, H. Luo, MOF-derived well-structured bimetallic catalyst for highly selective conversion of furfural, *Fuel* 289 (2021), 119910.
- F. Chen, K. Shen, Y. Yang, H. Huang, Y. Li, MOF-assisted synthesis of highly mesoporous Cr₂O₃/SiO₂ nanohybrids for efficient lewis-acid-catalyzed reactions, *ACS Appl. Mater. Interfaces* 12 (2020) 48691–48699.
- X. Chen, E. Yu, S. Cai, H. Jia, J. Chen, P. Liang, In situ pyrolysis of Ce-MOF to prepare CeO₂ catalyst with obviously improved catalytic performance for toluene combustion, *Chem. Eng. J.* 344 (2018) 469–479.
- J. Shen, X. Xu, J. Liu, Z. Liu, F. Li, R. Hu, J. Liu, X. Hou, Y. Feng, Y. Yu, Mechanistic understanding of metal phosphide host for sulfur cathode in high-energy-density lithium–sulfur batteries, *ACS Nano* 13 (2019) 8986–8996.
- W. Zhang, W. Ji, L. Li, P. Qin, I.E. Khalil, Z. Gu, P. Wang, H. Li, Y. Fan, Z. Ren, Exploring the fundamental roles of functionalized ligands in platinum@metal-organic framework catalysts, *ACS Appl. Mater. Interfaces* 12 (2020) 52660–52667.
- N. Tsumori, L. Chen, Q. Wang, Q.-L. Zhu, M. Kitta, Q. Xu, Quasi-MOF: exposing inorganic nodes to guest metal nanoparticles for drastically enhanced catalytic activity, *Chem* 4 (2018) 845–856.
- L. Fan, F. Zhao, Z. Huang, B. Chen, S.-F. Zhou, G. Zhan, Partial deligandation of M/Ce-BTC nanorods (M = Au, Cu, Au-Cu) with “Quasi-MOF” structures towards improving catalytic activity and stability, *Appl. Catal. A Gen.* 572 (2019) 34–43.
- P. Shi, Y. Zhang, Z. Yu, S. Zhang, Label-free electrochemical detection of ATP based on amino-functionalized metal-organic framework, *Sci. Rep.* 7 (2017) 6500.
- P. Shao, L. Ding, J. Luo, Y. Luo, D. You, Q. Zhang, X. Luo, Lattice-defect-enhanced adsorption of arsenic on zirconia nanospheres: a combined experimental and theoretical study, *ACS Appl. Mater. Interfaces* 11 (2019) 29736–29745.
- L. Ding, P. Shao, Y. Luo, X. Yin, S. Yu, L. Fang, L. Yang, J. Yang, X. Luo, Functionalization of UiO-66-NH₂ with rhodanine via amidation: towards a robust adsorbent with dual coordination sites for selective capture of Ag(I) from wastewater, *Chem. Eng. J.* 382 (2020), 123009.
- M. Liu, S. Li, N. Tang, Y. Wang, X. Yang, S. Wang, Highly efficient capture of phosphate from water via cerium-doped metal-organic frameworks, *J. Clean. Prod.* 265 (2020), 121782.
- J. Ding, Z. Yang, C. He, X. Tong, Y. Li, X. Niu, H. Zhang, UiO-66 (Zr) coupled with Bi₂MoO₆ as photocatalyst for visible-light promoted dye degradation, *J. Colloid Interfaces Sci.* 497 (2017) 126–133.
- Y. Gu, D. Xie, Y. Ma, W. Qin, H. Zhang, G. Wang, Y. Zhang, H. Zhao, Size modulation of zirconium-based metal organic frameworks for highly efficient phosphate remediation, *ACS Appl. Mater. Interfaces* 9 (2017) 32151–32160.
- Q. Wang, Y. Li, A. Serrano-Lotina, W. Han, R. Portela, R. Wang, M.A. Banares, K. L. Yeung, Operando investigation of toluene oxidation over 1D Pt@CeO₂ derived from Pt cluster-containing MOF, *J. Am. Chem. Soc.* 143 (2021) 196–205.
- J.L. Wang, X.F. Shi, L.W. Chen, H.Y. Li, M.Q. Mao, G.Y. Zhang, H. Yi, M.L. Fu, D. Q. Ye, J.L. Wu, Enhanced performance of low Pt loading amount on Pt-CeO₂ catalysts prepared by adsorption method for catalytic ozonation of toluene, *Appl. Catal. A Gen.* 625 (2021), 118342.
- R. Peng, S. Li, X. Sun, Q. Ren, L. Chen, M. Fu, J. Wu, D. Ye, Size effect of Pt nanoparticles on the catalytic oxidation of toluene over Pt/CeO₂ catalysts, *Appl. Catal. B Environ.* 220 (2018) 462–470.
- J.H. Lee, D.Y. Jo, J.W. Choung, C.H. Kim, H.C. Ham, K.Y. Lee, Roles of noble metals (M = Ag, Au, Pd, Pt and Rh) on CeO₂ in enhancing activity toward soot oxidation: active oxygen species and DFT calculations, *J. Hazard. Mater.* 403 (2021), 124085.
- Q. Yang, L. Li, X. Wang, Y. Ma, Tunable metal-support interaction of Pt/CeO₂ catalyst via surfactant-assisted strategy: insight into the total oxidation of CO and toluene, *J. Hazard. Mater.* 424 (2022), 127601.
- L. Nie, D. Mei, H. Xiong, B. Peng, Z. Ren, X.I.P. Hernandez, A. DeLaRiva, M. Wang, M.H. Engelhard, L. Kovarik, Activation of surface lattice oxygen in single-atom Pt/CeO₂ for low-temperature CO oxidation, *Science* 358 (2017) 1419–1423.
- L. Kuai, Z. Chen, S. Liu, E. Kan, N. Yu, Y. Ren, C. Fang, X. Li, Y. Li, B. Geng, Titania supported synergistic palladium single atoms and nanoparticles for room temperature ketone and aldehydes hydrogenation, *Nat. Commun.* 11 (2020) 1–9.

- [32] J. Jones, H. Xiong, A.T. DeLaRiva, E.J. Peterson, H. Pham, S.R. Challa, G. Qi, S. Oh, M.H. Wiebenga, X.I. Pereira Hernández, Thermally stable single-atom platinum-on-*ceria* catalysts via atom trapping, *Science* 353 (2016) 150–154.
- [33] D. Kunwar, S. Zhou, A. DeLaRiva, E.J. Peterson, H. Xiong, X.I. Pereira-Hernández, S.C. Purdy, R. ter Veen, H.H. Brongersma, J.T. Miller, Stabilizing high metal loadings of thermally stable platinum single atoms on an industrial catalyst support, *ACS Catal.* 9 (2019) 3978–3990.
- [34] J. Resasco, L. DeRita, S. Dai, J.P. Chada, M. Xu, X. Yan, J. Finzel, S. Hanukovich, A. S. Hoffman, G.W. Graham, Uniformity is key in defining structure-function relationships for atomically dispersed metal catalysts: the case of Pt/CeO₂, *J. Am. Chem. Soc.* 142 (2019) 169–184.
- [35] V.J. Cybulskis, J. Wang, J.H. Pazmiño, F.H. Ribeiro, W.N. Delgass, Isotopic transient studies of sodium promotion of Pt/Al₂O₃ for the water-gas shift reaction, *J. Catal.* 339 (2016) 163–172.
- [36] M.J. Kale, P. Christopher, Utilizing quantitative in situ FTIR spectroscopy to identify well-coordinated Pt atoms as the active site for CO oxidation on Al₂O₃-supported Pt catalysts, *ACS Catal.* 6 (2016) 5599–5609.
- [37] X. Liu, S. Jia, M. Yang, Y. Tang, Y. Wen, S. Chu, J. Wang, B. Shan, R. Chen, Activation of subnanometric Pt on Cu-modified CeO₂ via redox-coupled atomic layer deposition for CO oxidation, *Nat. Commun.* 11 (2020) 1–8.
- [38] Z. Ren, Y. Yang, S. Wang, X. Li, H. Feng, L. Wang, Y. Li, X. Zhang, M. Wei, Pt atomic clusters catalysts with local charge transfer towards selective oxidation of furfural, *Appl. Catal. B Environ.* 295 (2021), 120290.
- [39] X. Meng, L. Wang, L. Chen, M. Xu, N. Liu, J. Zhang, Y. Yang, M. Wei, Charge-separated metal-couple-site in NiZn alloy catalysts towards furfural hydrodeoxygenation reaction, *J. Catal.* 392 (2020) 69–79.
- [40] Q. Wang, J. Feng, L. Zheng, B. Wang, R. Bi, Y. He, H. Liu, D. Li, Interfacial structure-determined reaction pathway and selectivity for 5-(hydroxymethyl) furfural hydrogenation over Cu-based catalysts, *ACS Catal.* 10 (2019) 1353–1365.
- [41] F. Tang, L. Wang, M.D. Walle, A. Mustapha, Y.-N. Liu, An alloy chemistry strategy to tailoring the d-band center of Ni by Cu for efficient and selective catalytic hydrogenation of furfural, *J. Catal.* 383 (2020) 172–180.
- [42] X. Meng, Y. Yang, L. Chen, M. Xu, X. Zhang, M. Wei, A control over hydrogenation selectivity of furfural via tuning exposed facet of Ni catalysts, *ACS Catal.* 9 (2019) 4226–4235.
- [43] J. Yu, Y. Yang, L. Chen, Z. Li, W. Liu, E. Xu, Y. Zhang, S. Hong, X. Zhang, M. Wei, NiBi intermetallic compounds catalyst toward selective hydrogenation of unsaturated aldehydes, *Appl. Catal. B Environ.* 277 (2020), 119273.